Point spread function engineering for iris recognition system design

Amit Ashok[1,*] and Mark A. Neifeld[1,2]

[1]Department of Electrical and Computer Engineering, University of Arizona, Tucson, Arizona, 85721 USA

[2]College of Optical Sciences, University of Arizona, Tucson, Arizona, 85721 USA

*Corresponding author: ashoka@ece.arizona.edu

Received 3 September 2009; revised 15 January 2010; accepted 22 January 2010; posted 26 January 2010 (Doc. ID 116358); published 19 February 2010

Undersampling in the detector array degrades the performance of iris-recognition imaging systems. We find that an undersampling of 8×8 reduces the iris-recognition performance by nearly a factor of 4 (on CASIA iris database), as measured by the false rejection ratio (FRR) metric. We employ optical point spread function (PSF) engineering via a Zernike phase mask in conjunction with multiple subpixel shifted image measurements (frames) to mitigate the effect of undersampling. A task-specific optimization framework is used to engineer the optical PSF and optimize the postprocessing parameters to minimize the FRR. The optimized Zernike phase enhanced lens (ZPEL) imager design with one frame yields an improvement of nearly 33% relative to a thin observation module by bounded optics (TOMBO) imager with one frame. With four frames the optimized ZPEL imager achieves a FRR equal to that of the conventional imager without undersampling. Further, the ZPEL imager design using 16 frames yields a FRR that is actually 15% lower than that obtained with the conventional imager without undersampling.

OCIS codes: 110.1758, 100.3008, 070.5010, 100.4995.

1. Introduction

Many modern defense and security applications require automatic recognition and verification services that employ a variety of biometrics such as facial features, hand shape, voice, fingerprints, and iris. The iris is the annular region between the pupil and outer white sclera of the eye. Iris-based recognition has been gaining popularity in recent years, and it has several advantages compared to other traditional biometrics such as fingerprints and facial features. The iris-texture pattern represents a high density of information, and the resulting statistical uniqueness can yield false recognition rates as low as 1 in 10^{10} [1–3]. Further, it has been found that the human iris is stable over the lifetime of an individual and is therefore considered to be a reliable biometric [4]. Iris-based recognition systems rely on capturing the iris-texture pattern with a high-resolution imaging system. This places stringent demands on imaging optics and sensor design. Traditional high-resolution optical designs with small $F/\#$ result in a small depth-of-field, which limits the usable volume within which a successful image capture is possible. Several researchers have explored phase-mask based approaches to extend the depth-of-field of the high-resolution imaging systems employed for iris recognition [5–8]. Another design challenge with such imaging systems is that the overall imaging resolution can be limited by the undersampling in the detector array, and the resulting distortion can severely degrade the iris-recognition performance. Therefore, overcoming the detector-induced undersampling becomes a critical issue in design of an iris-recognition imaging system. In this paper, we will focus on addressing the detector-limited resolution in an iris-recognition imaging system design.

A natural approach to improve the imaging resolution beyond the detector limit, inspired by

0003-6935/10/100B26-14$15.00/0

the Papoulis's generalized sampling theorem [9], is to employ multiple subpixel shifted measurements within a TOMBO (thin observation module by bounded optics) imaging system architecture [10,11]. However, this approach does not exploit the optical degrees of freedom available to the designer, and more importantly, it does not address the specific nature of the iris-recognition task. Researchers have exploited the optical degrees of freedom to extend the depth-of-field of iris-recognition systems [5–8] as mentioned earlier, but we are not aware of any previous work that has examined undersampling in iris-recognition imaging systems specifically from this point of view. In this paper, we propose an approach that involves engineering the optical point spread function (PSF) of the imaging system in conjunction with use of multiple subpixel shifted measurements. It is important to note that the goal of our approach is to maximize the iris-recognition performance and not to increase the overall resolution of the imaging system directly. To accomplish this goal, we employ an optimization framework to engineer the optical PSF and optimize the postprocessing system parameters. The performance metric used within our optimization framework is false rejection ratio (FRR) for a given fixed false acceptance ratio (FAR) [12]. This task-specific metric is key to our design method and represents the design goal of maximizing the iris-recognition performance directly. The mechanism of modifying the optical PSF employs a phase mask in the aperture stop of the imaging system. This phase mask is defined with Zernike polynomials, and the coefficients of these polynomials serve as the optical design parameters. The aforementioned optimization framework is used to design imaging systems for various numbers of subpixel shifted measurements. The CASIA iris database [13] is used in the optimization framework and also serves to quantify the performance of the resulting optimized imaging system designs.

2. Imaging System Model

In this study, an iris-recognition imaging system is composed of three components: (1) the optical imaging system, (2) the reconstruction algorithm, and (3) the recognition algorithm. The optical imaging system consists of multiple subapertures with identical optics. This multiaperture imaging system produces a set of subpixel shifted images on the detector array similar to a TOMBO imaging system. The task of the reconstruction algorithm is to combine these image measurements to form an estimate of the object. Finally, the iris-recognition algorithm operates on this object estimate and either accepts or rejects the iris as a match. We begin by describing the multiaperture imaging system.

A. Multiaperture Imaging System

Figure 1 shows the system layout of the multiaperture (MA) imaging system. The number of subimagers comprising the MA imaging system is denoted by K. The detector array in the focal plane of the MA imager generates K image measurements, where the kth measurement (also referred to as a frame) is denoted by $\mathbf{g}_k$. The detector pitch d of the detector array relative to the Nyquist sampling interval δ, determined by the optical cutoff spatial frequency ρ_c, defines the undersampling factor: $F = d/\delta \times d/\delta$. Therefore, for an object of size $N \times N$ pixels the kth subimager produces an undersampled measurement $\mathbf{g}_k$ of dimension $M \times M$, where $M = \lceil N/\sqrt{F} \rceil$. Mathematically, the kth frame can be expressed as

$$\mathbf{g}_k = \mathbf{H}_k \mathbf{f} + \mathbf{n}_k, \tag{1}$$

where $\mathbf{f}$ is a $N^2 \times 1$ dimensional vector formed by a lexicographic arrangement of a two-dimensional $(N \times N)$ discretized representation of the object, $\mathbf{H}_k$ is the $M^2 \times N^2$ discrete-to-discrete imaging operator of the kth subimager, and $\mathbf{n}_k$ denotes the $M^2 \times 1$ dimensional measurement error vector. Here we model the measurement error $\mathbf{n}_k$ as zero-mean additive white Gaussian noise (AWGN) with variance σ_n^2. Note that the imaging operator $\mathbf{H}_k$ is different for each subimager and is expressed as

$$\mathbf{H}_k = \mathbf{DCS}_k, \tag{2}$$

where $\mathbf{S}_k$ is the $N^2 \times N^2$ shift operator that produces a two-dimensional subpixel shift $(\Delta X_k, \Delta Y_k)$ in the kth subimager, $\mathbf{C}$ is $N^2 \times N^2$ convolution operator that represents the optical PSF, and $\mathbf{D}$ is the $M^2 \times N^2$

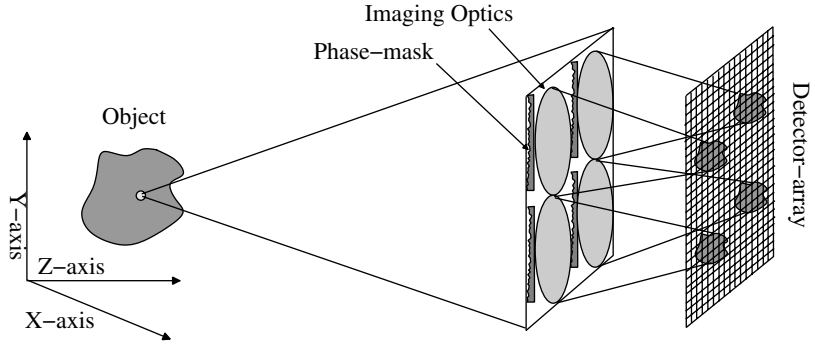

Fig. 1. PSF-engineered multiaperture imaging system layout.

downsampling operator, which includes the effect of spatial integration over the detector and the undersampling caused by the detector array. Note that the convolution operator $\mathbf{C}$ does not vary with k because the optics are assumed to be identical in all subimagers. By combining the K measurements we can form a composite measurement $\mathbf{g} = \{\mathbf{g}_1\mathbf{g}_2\ldots\mathbf{g}_K\}$ that can be expressed in terms of the object vector $\mathbf{f}$ as follows:

$$\mathbf{g} = \mathbf{H}_c\mathbf{f} + \mathbf{n}, \tag{3}$$

where $\mathbf{H}_c = \{\mathbf{H}_1\mathbf{H}_2\cdots\mathbf{H}_K\}$ is the composite imaging operator of size $KM^2 \times N^2$ obtained by stacking the K imaging operators corresponding to each of the K subimagers and $\mathbf{n}$ is the composite noise vector defined as $\mathbf{n} = \{\mathbf{n}_1\mathbf{n}_2\ldots\mathbf{n}_K\}$.

As mentioned earlier, the optical PSF is engineered by placing a phase mask in the aperture stop of each subimager. The pupil function $t_{\text{pupil}}(\rho,\theta)$ of each subimager is expressed as [14]

$$t_{\text{pupil}}(\rho,\theta) = t_{\text{amp}}(\rho)\exp\left(\frac{j2\pi(n_r-1)t_{\text{phase}}(\rho,\theta)}{\lambda}\right), \tag{4}$$

where ρ and θ are the polar coordinates, n_r is the refractive index of the phase mask, $t_{\text{amp}}(\rho) = \text{circ}\left(\rho/D_{ap}\right)$ is the circular pupil-amplitude function (D_{ap} denotes the aperture diameter), $t_{\text{phase}}(\rho,\theta)$ represents the pupil-phase function (i.e. phase-mask profile), and λ is the wavelength. A Zernike polynomial of order P is used to define the pupil-phase function as follows:

$$t_{\text{phase}}(\rho,\theta) = \sum_{i=1}^{P} a_i \cdot Z_i(\rho,\theta), \tag{5}$$

where a_i is the coefficient of the ith Zernike polynomial denoted by $Z_i(\rho,\theta)$ [15]. In this paper, we will use Zernike polynomials with terms up to $P = 24$. The resulting optical PSF $h(\rho,\theta)$ is expressed as [16]

$$h(\rho,\theta) = \frac{A_c}{(\lambda f_l)^4}\left|T_{\text{pupil}}\left(-\frac{\rho}{\lambda f_l},\theta\right)\right|^2, \tag{6}$$

$$T_{\text{pupil}}(\boldsymbol{\omega}) = \mathcal{F}_2\{t_{\text{pupil}}(\rho,\theta)\}, \tag{7}$$

where $\boldsymbol{\omega}$ is the two-dimensional spatial frequency vector, A_c is a normalization constant with units of area, f_l is the back focal length, and $\mathcal{F}_2$ denotes the two-dimensional forward Fourier transform operator.

A discrete representation of the optical PSF $h_d(l,m)$, required for defining the $\mathbf{C}$ operator, is obtained as follows:

$$h_d(l,m) = \int_{-\frac{d}{2}}^{\frac{d}{2}}\int_{-\frac{d}{2}}^{\frac{d}{2}} h(x-ld, y-md)\,dx\,dy\{(l,m): l = -L\ldots L, m = -L\ldots L\}, \tag{8}$$

where $(2L+1)^2$ is the number of samples used to represent the optical PSF. Note that a lexicographic ordering of the $h_d(l,m)$ yields one row of $\mathbf{C}$ and all other rows are obtained by lexicographically ordering the appropriately shifted version of this discrete optical PSF.

B. Reconstruction Algorithm

The measurements from the K subimagers comprising the MA imaging system form the input to the reconstruction algorithm. We employ a reconstruction algorithm based on the linear minimum mean square error (LMMSE) criteria. The LMMSE method is essentially a generalized form of the Wiener filter, and it operates on the measurement in the spatial domain without the assumption of shift invariance. Given the imaging model specified in Eq. (3) the LMMSE spatial operator $\mathbf{W}$ can be written as [17]

$$\mathbf{W} = \mathbf{R}_{\mathbf{ff}}\mathbf{H}_c^T(\mathbf{H}_c\mathbf{R}_{\mathbf{ff}}\mathbf{H}_c^T + \mathbf{R}_{\mathbf{nn}})^{-1}, \tag{9}$$

where $\mathbf{R}_{\mathbf{ff}}$ is the object autocorrelation matrix and $\mathbf{R}_{\mathbf{nn}}$ is the noise autocorrelation matrix. Here we assume that noise is zero-mean AWGN with variance σ_n^2 and therefore $\mathbf{R}_{\mathbf{nn}} = \sigma_n^2\mathbf{I}$. Note that for an object of size N^2 and measurement of size KM^2, the size of the $\mathbf{W}$ matrix is $N^2 \times KM^2$. For even a modest object size of 280×280, as is the case for the work reported herein, computing the $\mathbf{W}$ matrix becomes intractable. Therefore, we adopt an alternate approach that does not rely on directly computing matrix inverses but instead uses a conjugate-gradient method to compute the LMMSE solution iteratively. Before we describe the iterative algorithm, we first need a method to estimate the object autocorrelation matrix $\mathbf{R}_{\mathbf{ff}}$. Note that the object of interest in the iris-recognition task is the iris itself. This suggests that the object autocorrelation should only include the iris statistics; however, it is important to note that the iris can only be located in the context of other local features such as outer sclera, eyelashes, and eyebrow. Therefore, we include all regions in the iris sample images for estimating the object autocorrelation matrix. A training set of 40 subjects with 4 iris samples for each subject, randomly selected from the CASIA iris database, yields a total of 160 iris object samples. Figure 2 shows example iris objects from the training dataset. The kth iris object yields the sample autocorrelation function $r_{\mathbf{ff}}^k$, which is used to estimate the actual autocorrelation function as follows:

$$\hat{R}_{\mathbf{ff}} = \frac{1}{160}\sum_{k=1}^{160} r_{\mathbf{ff}}^k. \tag{10}$$

The corresponding estimated power spectral density $\hat{\mathbf{S}}_{\mathbf{ff}}$ can be written as [18]

$$\hat{\mathbf{S}}_{\mathbf{ff}}(\rho) = \mathcal{F}_2(\hat{\mathbf{R}}_{\mathbf{ff}}). \tag{11}$$

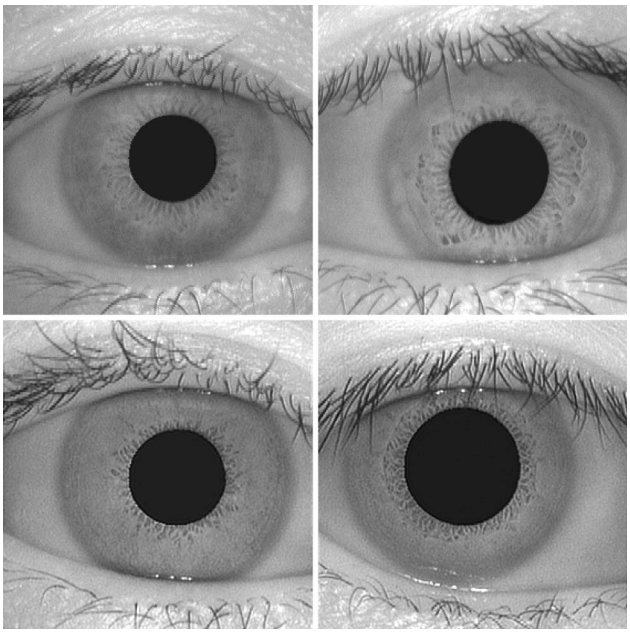

Fig. 2. Iris examples from the training dataset.

To obtain a smooth approximation, we use the following parametric function $\mathbf{S_{ff}}$ to fit to the estimated power spectral density $\hat{\mathbf{S}}_{\mathbf{ff}}$ [19,20]:

$$\mathbf{S_{ff}}(\rho) = \frac{\sigma_f^2}{(1 + 2\pi\mu_d\rho^2)^{\frac{3}{2}}}. \tag{12}$$

Note that because the iris is circular, we assume a radially symmetric power function $\mathbf{S_{ff}}$. A least square fit to $\hat{\mathbf{S}}_{\mathbf{ff}}(\rho)$ yields a $\sigma_f = 43589$ and $\mu_d = 0.489$. A radial profile of the object power spectral density estimated from the training set along with parametric fit defined in Eq. (12) are shown in Fig. 3.

In general, a conjugate-gradient algorithm minimizes the following form of quadratic objective function Q [16]:

$$Q(\hat{\mathbf{f}}) = \frac{1}{2}\hat{\mathbf{f}}^t\mathbf{A}\hat{\mathbf{f}} - \mathbf{b}^t\hat{\mathbf{f}}. \tag{13}$$

For the LMMSE criteria, $\mathbf{A} = \mathbf{H}_c^T\mathbf{H}_c + \sigma^2\mathbf{R}_{\mathbf{ff}}^{-1}$ and $\mathbf{b} = \mathbf{H}_c^T\mathbf{g}$. Within our iterative conjugate gradient-based algorithm we use a conjugate vector $\mathbf{p}_j$ instead of the gradient of the objective $Q(\hat{\mathbf{f}})$ to achieve a faster convergence to the LMMSE solution [21]. The $(k+1)$th update rule can be expressed as [16]

$$\hat{\mathbf{f}}^{k+1} = \hat{\mathbf{f}}^k + \alpha^k\mathbf{p}_k, \tag{14}$$

$$\alpha^k = -\frac{\mathbf{p}_k^t\nabla Q^k}{d_k}, \tag{15}$$

where ∇Q^k denotes the gradient of objective function Q^k evaluated at the kth step and $\mathbf{p}_k$ is conjugate to all previous $\mathbf{p}_j, j < k$ (i.e., $\mathbf{p}_j^t\mathbf{A}\mathbf{p}_k = d_j\delta_{jk}$), δ_{jk} is the Kronecker-delta function, and d_k is the $\|\cdot\|_2$ norm of the $\mathbf{p}_k$ vector. The stopping criteria is specified to be when the residual vector $\mathbf{r}_k = \nabla Q^k = \mathbf{A}\hat{\mathbf{f}}^k - \mathbf{b}$ changes less than $\beta\%$ over the last iteration (i.e., $(\mathbf{r}_{k-1} - \mathbf{r}_k)/\mathbf{r}_{k-1} \le \beta/100$).

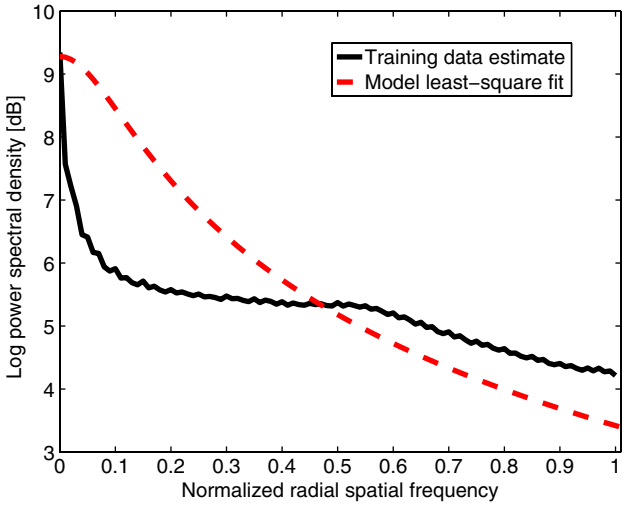

Fig. 3. (Color online) Model fit and training estimate of the object power spectral density: a radial profile.

C. Iris-Recognition Algorithm

The object estimate obtained with the reconstruction algorithm is processed by the iris-recognition algorithm to make the final decision. There are three main processing steps that form the basis of the iris-recognition algorithm. The first step involves a segmentation algorithm that extracts the iris, pupil, and eyelid regions from the reconstructed object. The segmentation algorithm used in this paper is adapted from Ref. [22] with the addition of eyelid boundary detection. The output of the segmentation algorithm yields an estimate of the center and radius of the circular pupil and iris regions and also the boundaries of the upper and lower eyelids in the object. Figure 4(a) shows an example iris image that was processed with the segmentation algorithm. The pupil and iris regions are outlined by circular boundaries, and the upper/lower eyelid edges are represented by the elliptical boundaries. This information is used to generate a mask $M(x,y)$ that extracts the annular region between iris and pupil boundaries that contains only the unobscured iris-texture region. An example of the masked iris region is shown in Fig. 4(b). The extracted iris-texture region is the input to the next processing step. Given the center and radius of the pupil and the iris regions, the annular iris-texture region is unwrapped into a rectangular area $a(\rho,\theta)$ using Daugman's homogenous rubber sheet model [23]. The size of the rectangular region is specified as $L_\rho \times L_\theta$ with L_ρ rows along the radial direction and L_θ columns along the angular direction. Figure 4(c) shows an example of an unwrapped rectangular region with $L_\rho = 36$ and $L_\theta = 224$. In the next step, a complex log-scale Gabor filter is applied to each row to extract the phase of the underlying iris-texture pattern. The complex log-scale Gabor filter spectrum $G_{\log}(\rho)$ is defined as [24]

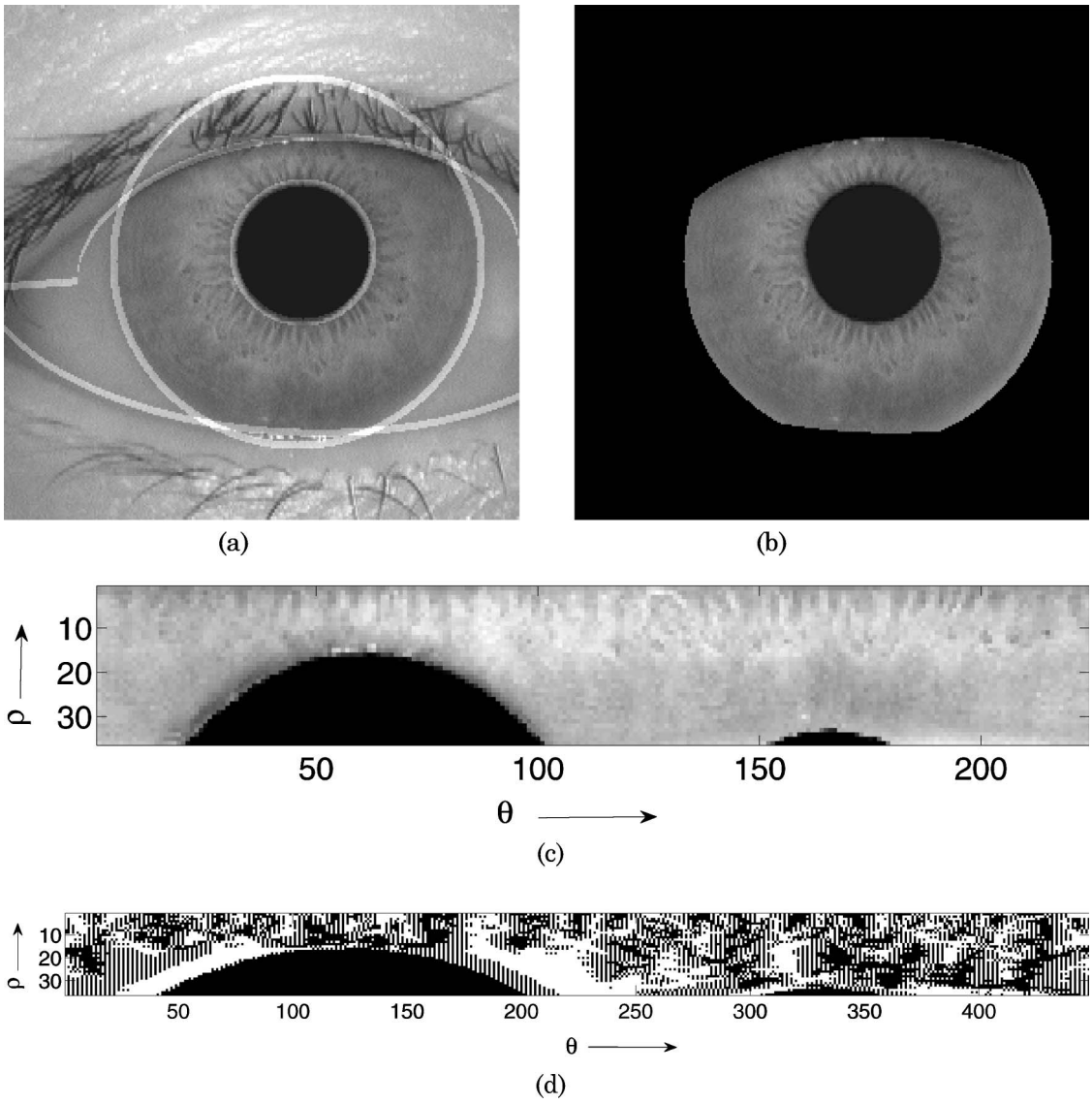

Fig. 4. Examples of (a) iris segmentation, (b) masked iris texture region, (c) unwrapped iris, and (d) iris code.

$$G_{\log}(\rho) = \exp\left(-\frac{\log\left(\frac{\rho}{\rho_o}\right)}{2\log\left(\frac{\sigma_g}{\rho_o}\right)}\right), \qquad (16)$$

where ρ_o is the center frequency of the filter and σ_g specifies its bandwidth. Note that this filter is only applied along the angular direction, which corresponds to pixels along the circumference of a circle in the original object. The angular direction is chosen over the radial direction because the maximum texture variation occurs along this direction [22]. The phase of the complex output of each Gabor filter is then quantized into four quadrants using two bits. The four-level quantized phase is coded using a Grey code so that the difference between any two adjacent quadrants is one bit. This Grey coding scheme ensures that any misalignment between two similar iris codes results in a minimum of errors. The quantized phase results in a binary pattern, shown in Fig. 4(d), which is referred to as an "iris code."

In the final step, the iris-recognition task is performed based on the iris code obtained from the test object. To determine whether the given iris code denoted by t_{code} matches any iris code in the database a score is computed. The score denoted by $s(t_{\text{code}})$ is defined as

$$s(t_{\text{code}}) = \min_{k,i} d_{hd}(t_{\text{code}} c^k_{\text{mask}}, R_i(r^k_{\text{code}}) c^k_{\text{mask}}), \qquad (17)$$

where r^k_{code} is the kth reference iris code in the database, c^k_{mask} is a mask that represents the unobscured bits common among the test and the reference iris codes, R_i is a shift operator which performs an i-pixel circular shift along the angular direction, and d_{hd} is the Hamming distance operator. All shifts in the range $\{i : -O \ldots +O\}$ are considered, where O denotes the maximum shift. The d_{hd} operator is defined as follows:

$$d_{hd}(t_{\text{code}}c_{\text{mask}}, r_{\text{code}}c_{\text{mask}}) = \frac{\sum(t_{\text{code}}c_{\text{mask}} \oplus r_{\text{code}}c_{\text{mask}})}{W}, \tag{18}$$

where W is the weight (i.e., number of all 1's) of the mask c_{mask}, and the $\oplus$ symbol denotes the XOR operation. The normalized Hamming distance score defined in Eq. (18) is computed over all iris codes in the database. The iris code is shifted to account for any rotation of the iris in the object. Finally, the following decision rule is applied to the minimum iris score $s(t_{\text{code}})$:

$$s(t_{\text{code}}) \underset{H_1}{\overset{H_0}{\lessgtr}} T_{HD}, \tag{19}$$

which translates to: accept the null hypothesis H_0 if the score is less than threshold T_{HD}; otherwise accept the alternative hypothesis H_1. The null hypothesis H_0 is that the test iris code is a match, and the alternate hypothesis H_1 indicates that no match was found. The threshold T_{HD} determines the performance of the iris-recognition system as summarized by the FRR and FAR statistics. Note that for a fixed FAR the T_{HD} value is chosen so as to minimize the FRR statistics, and therefore T_{HD} cannot be considered a free parameter in the iris-recognition algorithm.

3. Optimization Framework

The goal of our optimization framework is to enable the design of an iris-recognition system that minimizes FRR for a fixed FAR in the presence of undersampling. Figure 5 illustrates the definitions of FRR and FAR in the context of intraclass distance and interclass distance probability densities. The intraclass distance refers to the set of distances between iris codes of the same subject, whereas the interclass distance refers to the set of distances between iris codes of different subjects. The rationale behind this choice of performance metric is that the cost/risk of not recognizing an iris that is actually enrolled (defined as false rejection error, which is a type II error) in the database is far greater than the cost/risk of recognizing an iris as a match when it is not enrolled in the database (defined as false acceptance error, a type I error) in a "search" type security application. In these applications the main task is to identify certain subject(s) in a general population. Note that the FRR and FAR errors cannot be reduced simultaneously. In this study we set FAR to 0.001. We recognize that this specific FAR value may not represent an optimal choice for an actual system implementation, however; here it only serves as a representative value in our optimization framework.

In the MA imaging system the coefficients of the Zernike polynomials, which describe the pupil-phase function, represent the optical design parameters. The parameters of the reconstruction algorithm (β) and the iris-recognition algorithm $(\rho_o, \sigma_g, L_\rho, L_\theta, O)$ comprise the degrees of freedom available in the computational domain. Ideally, a joint optimization of the optical and the postprocessing parameters would yield the maximum iris-recognition performance. However, the resulting optimization process becomes computationally intractable due to the high computational complexity of evaluating the objective function coupled with the large number of design variables. To understand the computational complexity of the objective function itself, consider that its computation involves the estimation of the intraclass and interclass iris distance probability densities. This requires computing iris codes from a large set of reconstructed iris objects and comparing them to the reference iris database. In this paper, we use a training dataset with 160 iris object samples,

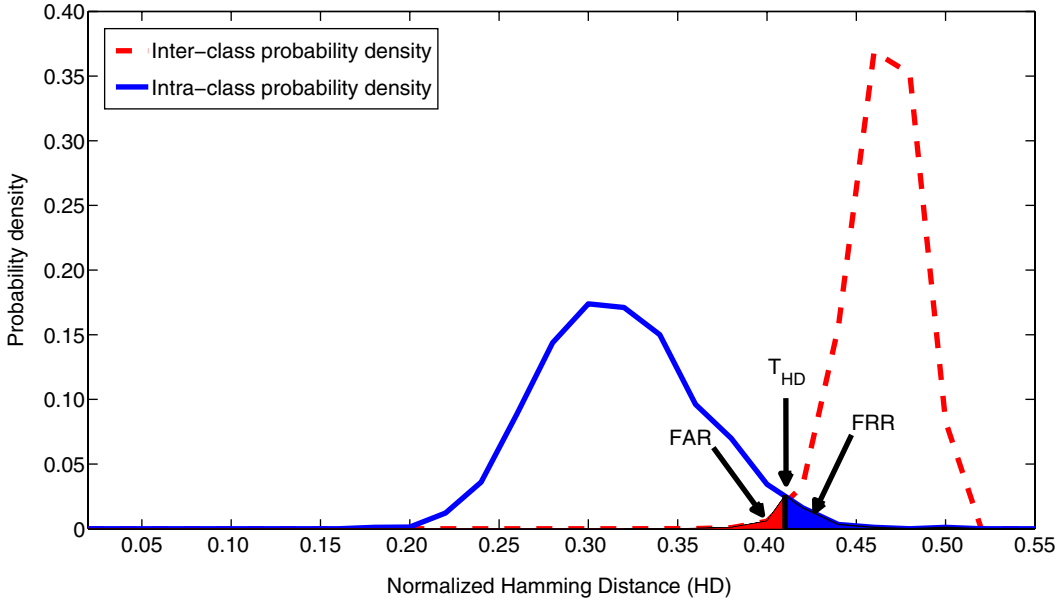

Fig. 5. (Color online) Illustration of FRR and FAR definitions in the context of intraclass and interclass probability densities.

Table 1. Imaging System Performance (FRR) for $K = 1$, $K = 4$, $K = 9$, and $K = 16$ on Training Dataset

Undersampling	Frames	TOMBO	Defocus TOMBO	ZPEL
$F = 1 \times 1$	Conventional imager	0.133		
$F = 8 \times 8$	$K = 1$	0.458	0.360 (21.4%)	0.295 (35.6%)
$F = 8 \times 8$	$K = 4$	0.153	0.139 (9.2%)	0.128 (16.3%)
$F = 8 \times 8$	$K = 9$	0.140	0.136 (2.9%)	0.117 (16.4%)
$F = 8 \times 8$	$K = 16$	0.135	0.142 (−5.2%)	0.113 (16.3%)

described in Subsection 2.B. In order to generate a statistically reliable estimate of the interclass and intraclass distance probability densities, we need to generate a large set of iris-code samples. This is achieved by simulating an iris object for 10 random noise realizations yielding as many iris codes for each iris object. Thus, a single evaluation of the objective function effectively results in simulation of 1600 iris objects through the imaging system.

In our optimization framework, we adopt an alternative approach that reduces the computational complexity by splitting the optimization into two separate steps. Note that the iris-recognition algorithm parameters are inherently a function of the iris-texture statistics and are not strongly dependent on the optics. For example, the center frequency and the bandwidth of the log Gabor filter are tuned to the spatial frequency distribution of the iris-texture that contains the most discriminating information. Further, the parameters L_ρ and L_θ are dependent on the correlation length of the iris texture along radial and angular directions respectively. This observation allows us to separate the optimization of the iris-recognition algorithm parameters from the optimization of the optics and the reconstruction algorithm. Therefore, the first optimization step involves optimizing the iris-recognition algorithm parameters to minimize the FRR. For this step, the detector pitch is chosen such that there is no undersampling and there is no phase mask within the imaging optics. The optimization is performed with a coarse-to-fine search method using the iris objects from the training dataset. It is found that $L_\rho = 36$, $L_\theta = 224$, $\rho_o = 1/18$, and $\sigma_g = 0.4$ yield the optimal performance. The number of left and right shifts required to achieve optimal performance is found to be $O = 8$ in each direction. The second optimization step involves the optimization of optical and reconstruction algorithm parameters, which has significantly reduced computational complexity as a result of fewer number of design variables involved. The optical system parameters include the P coefficients of the Zernike polynomials. The reconstruction algorithm parameter β, associated with the stopping condition in the iterative conjugate-gradient algorithm, is the only postprocessing design variable used in this optimization step. Note that the value of iris-recognition algorithm parameters remain fixed during this optimization step.

Our optimization framework employs a simulated tunneling algorithm, a global optimization technique [25], to perform the second optimization step.

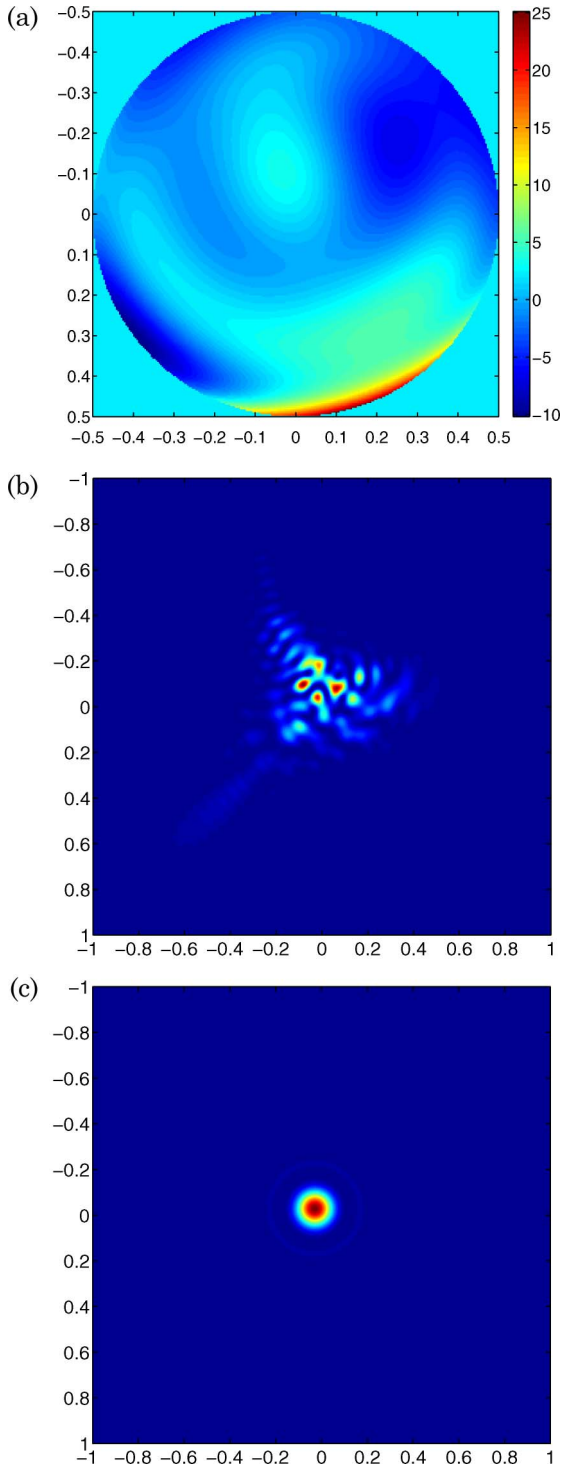

Fig. 6. (Color online) Optimized ZPEL imager with $K = 1$ (a) pupil phase, (b) optical PSF, and (c) optical PSF of the TOMBO imager.

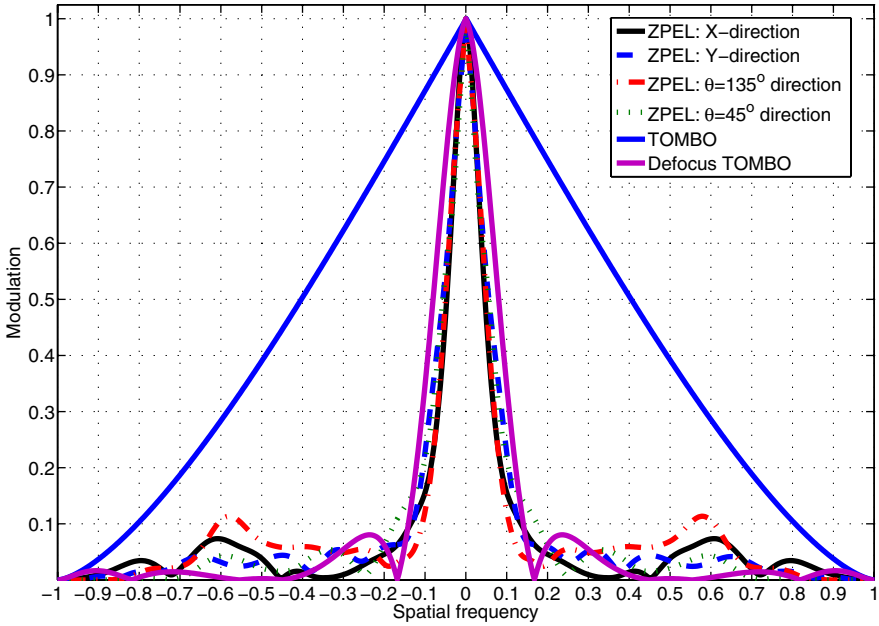

Fig. 7. (Color online) Cross-section MTF profiles of optimized ZPEL imager with $K = 1$.

Simulated tunneling optimization, based on the well known simulated annealing global optimization technique, modifies the local energy surface to allow "tunneling" through local objective function extrema akin to physical phenomenon of quantum tunneling, thereby accelerating the optimization process. The global optimization algorithm is implemented in a message passing interface (MPI) based environment [26] that allows it to run on multiple processors in parallel, thereby significantly decreasing the computation time required for each iteration. The simulated tunneling algorithm is run for sufficient iterations until a convergence is achieved (we observe that empirically 4000 to 5000 iterations are usually sufficient to achieve convergence). Multiple runs of the optimization algorithm with random initialization yielded similar results, giving us confidence that the optimization results are global.

This optimization framework is used to design imaging systems with an undersampling factor of $F = 8 \times 8$, employing $K = 1$, $K = 4$, $K = 9$, and $K = 16$ frames. The subpixel shifts for K frames is chosen as multiples of $\Delta = d/\sqrt{K}$ along each direction, where d is the detector pitch/size [27,28]. For example, for $K = 4$ the subpixel shifts are $\left\{(\Delta_X, \Delta_Y) : (0,0), \left(d/2, 0\right), \left(0, d/2\right), \left(d/2, d/2\right)\right\}$. The noise variance σ_n^2 is set so that the measurement signal to noise ratio (SNR) is equal to 56 dB for the undersampled imager with $K = 1$. Henceforth, an optimized PSF engineered imaging system will be referred to as the Zernike phase-enhanced lens (ZPEL) imaging system. In Section 4, we discuss the performance of the optimized ZPEL imager and compare it the corresponding TOMBO imaging system employing the same number of frames. Note that while the TOMBO imaging system does not use PSF engineering (instead it uses conventional imaging optics), the reconstruction algorithm parameter β is still optimized to achieve the minimum FRR.

Table 2. TOMBO Imaging System Performance (FRR) with Defocus and $K = 1$ on Training Dataset

Defocus	FRR
$W_d = 1$	0.446
$W_d = 2$	0.437
$W_d = 3$	0.432
$W_d = 4$	0.401
$W_d = 5$	0.396
$W_d = 6$	0.382
$W_d = 7$	0.360
$W_d = 8$	0.363
$W_d = 9$	0.492

4. Results and Discussion

As mentioned earlier, undersampling in the detector array degrades the performance of the iris-recognition imaging system. Specifically we find that an undersampling factor of $F = 8 \times 8$ yields a FRR = 0.458 as compared to FRR = 0.133 without undersampling in the conventional imaging system. This represents a significant reduction in performance and highlights the need to mitigate the effect of undersampling. Increasing the number of subpixel shifted frames from $K = 1$ to $K = 16$ improves the performance of the TOMBO imaging system, as evident from the FRR data shown in Table 1. To ensure a fair comparison among imaging systems with various numbers of frames, we enforce a total photon constraint. This constraint implies that the total number of photons available to each imager (i.e., summed over all frames) is fixed. Therefore, for an

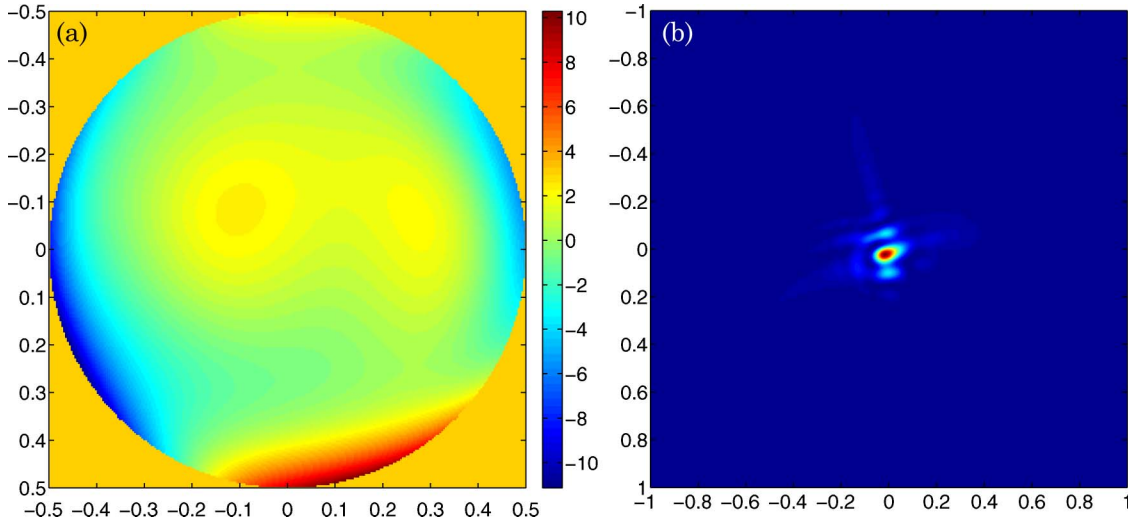

Fig. 8. (Color online) Optimized ZPEL imager with $K = 4$: (a) pupil phase and (b) optical PSF.

imaging system using K frames the measurement noise variance must be scaled by a factor of K. For example, the measurement noise variance in an imaging system with $K = 4$ frames is set to $\sigma_K^2 = 4\sigma_n^2$, where σ_n^2 is the measurement noise variance of the imaging system with $K = 1$. Subject to this constraint, we expect that a ZPEL imaging system designed within the proposed optimization framework would improve upon the performance of the TOMBO imaging system.

We begin by examining the result of optimizing the ZPEL imaging system with $K = 1$. Figure 6(a) shows the optimized Zernike phase mask, and Fig. 6(b) shows the corresponding optical PSF of the ZPEL imager. For the purpose of comparison, Fig. 6(c) shows the optical PSF of the TOMBO imager. The phase mask spans over the extent of the aperture stop, where 0.5 corresponds to the radius $\left(D_{ap}/2\right)$ of the aperture. The optical PSF is plotted on a normalized scale of $[-1, 1]$, where 1 corresponds to the detector size d that results in the $F = 8 \times 8$ undersampling. Note that the large spatial extent of the PSF relative to that of a TOMBO imaging system suggests that high spatial frequencies in the corresponding modulation transfer function (MTF) would be suppressed. Figure 7 shows plots of various cross sections of the two-dimensional MTF for the ZPEL and TOMBO imagers. Here the spatial frequency is plotted on the normalized scale of $[0, 1]$, where 1 corresponds to the optical cutoff frequency ρ_c. Observe that the ZPEL MTF reduces rapidly with increasing spatial frequency. This can be understood as the optimization process suppressing the MTF at the high spatial frequencies to reduce the effect of aliasing. However, notice that the nonzero MTF at midspatial frequencies still allows the reconstruction algorithm to potentially recover some information in this region that is relevant to the iris-recognition task. Given these observations, it is compelling to consider the possibility that by simply defocusing the imaging optics of a TOMBO imager by the correct amount, a similar MTF and therefore a similar performance might be obtained. This is indeed the case, although only to a limited extent, as evident from the FRR data shown in Table 2. These data are obtained by computing the TOMBO imager performance at various values of defocus, denoted by the defocus parameter W_d (this defocus parameter is directly proportional to the coefficient of the third element of the Zernike polynomial expansion [15]). The optimal value of defocus parameter gives the minimum FRR value. In this case, the optimal defocus parameter value of $W_d = 7.0$ yields a FRR $= 0.360$. This represents an improvement of 21.4% over the TOMBO imager performance. However, the ZPEL imaging system with a FRR $= 0.295$ represents an additional improvement of 18% over the optimal defocus TOMBO imaging system's performance and an improvement of 35.6% relative to the TOMBO imaging system. This performance difference between the optimal defocus TOMBO imager and the ZPEL imager can be understood by closely examining their MTFs as shown in Fig. 7. Note that unlike the MTF of the ZPEL imaging system, the defocus TOMBO imaging system's MTF has several nulls and near zero modulation at high-spatial frequencies. From this observation we may infer that, while it is important to selectively lower the MTF at high-spatial frequencies to minimize the effect of aliasing, it is also important to minimize the nulls in the optimized MTF that lead to information loss.

For the imaging system utilizing $K = 4$ frames, the optimized ZPEL imager yields a FRR $= 0.128$ that is 16.3% lower than FRR $= 0.153$ of the TOMBO imaging system. Figures 8(a) and 8(b) show the phase mask and the optical PSF of this optimized ZPEL imager, respectively. Note that the optical PSF has a smaller extent compared to that for $K = 1$. The use of four frames as opposed to one frame reduces the effective undersampling by a factor of 2 in each

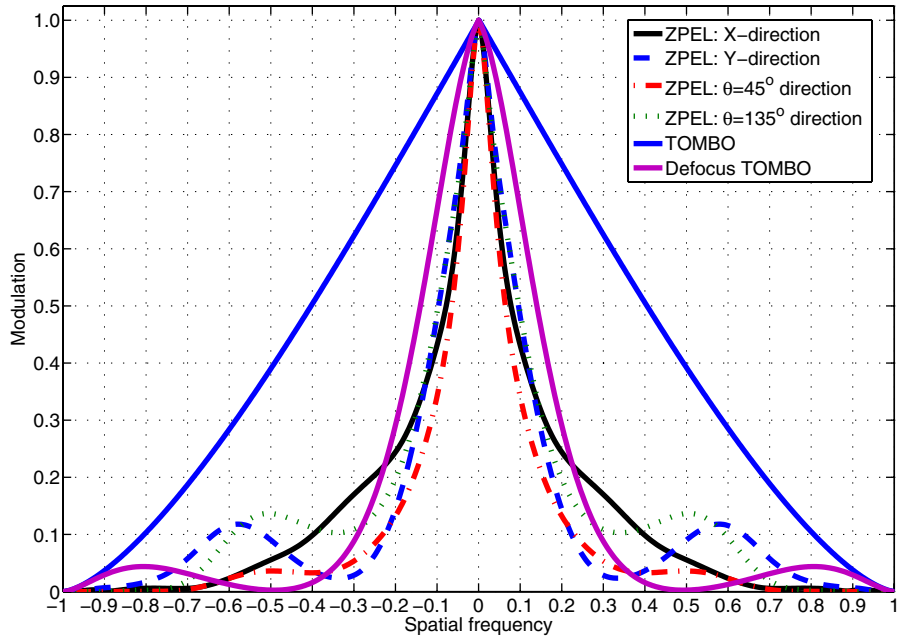

Fig. 9. (Color online) Cross-section MTF profiles of optimized ZPEL imager with $K = 4$.

direction. Thus we expect as a result, the MTF in this case is higher especially in the midspatial frequencies compared to the MTF of the ZPEL imager with $K = 1$. This is confirmed by the plot of the ZPEL MTF in Fig. 9. It is also interesting to note that while the optimal defocus TOMBO imager design ($W_d = 4$) is able to achieve a FRR $= 0.139$, an improvement of 9.1% over the FRR of a TOMBO imager, it still significantly worse (the FRR improvement is lower by nearly a factor of 2) than the optimized ZPEL imager design. Another important observation is that the FRR $= 0.128$ achieved by the optimized ZPEL imager is actually lower than FRR $= 0.133$ of the conventional imaging system without any undersampling. This clearly highlights the effectiveness of the optimization framework used for ZPEL imager designs, which not only overcomes the performance degradations introduced by detector undersampling but also successfully incorporates the object statistics relevant to the iris-recognition task to enhance the performance beyond that of the conventional imager.

Figures 10(a) and 10(b) show the Zernike phase mask and the optical PSF of the optimized ZPEL imager with $K = 9$. The ZPEL imager achieves a FRR $=$ 0.117 compared to FRR $= 0.140$ for the TOMBO imaging system, an improvement of 16.4%. The MTF of this imaging system is shown in Fig. 11. The optimal defocus TOMBO imager design ($W_d = 0.75$) is only able to achieve a marginal improvement of 2.9% with an FRR $= 0.136$ relative to the TOMBO imaging system design. The optimized ZPEL imager with $K = 16$ frames reduces it further to FRR $= 0.113$,

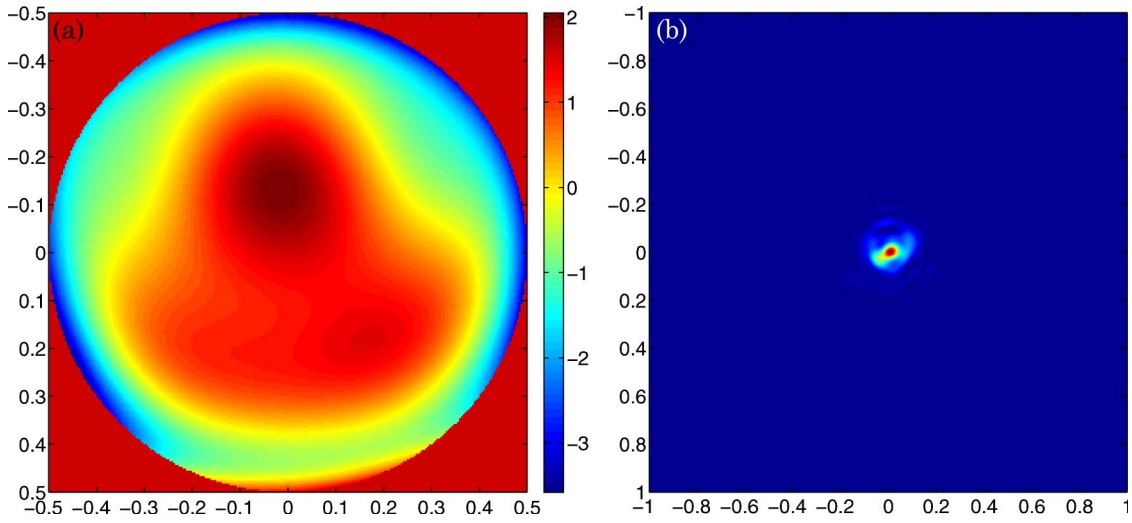

Fig. 10. (Color online) Optimized ZPEL imager with $K = 9$: (a) pupil phase and (b) optical PSF.

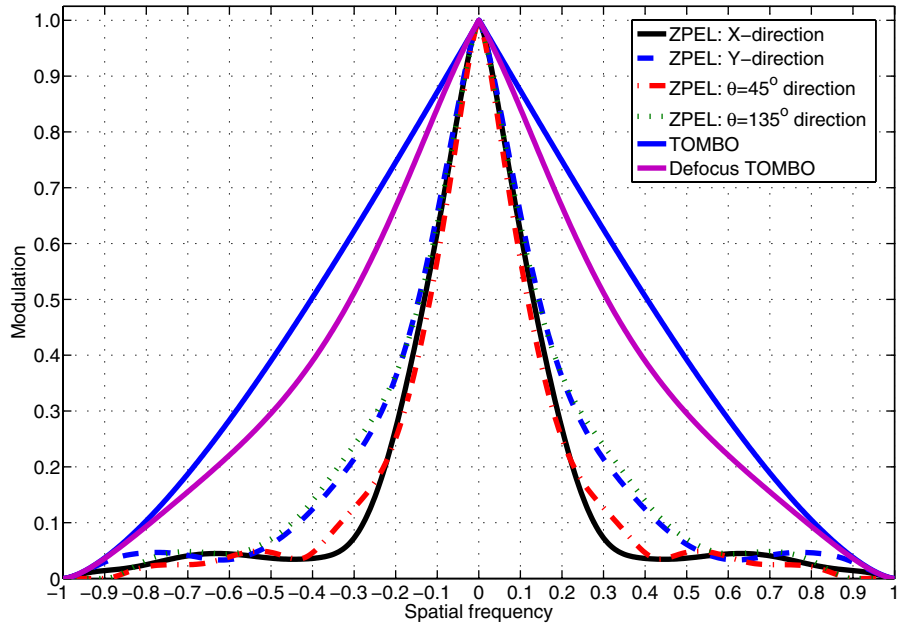

Fig. 11. (Color online) Cross-section MTF profiles of optimized ZPEL imager with $K = 9$.

an improvement of 16.3% over FRR = 0.135 of the TOMBO imaging system with the same number of frames. The Zernike phase mask, the optical PSF, and the MTF of this ZPEL imager are shown in Figs. 12(a), 12(b), and 13, respectively. In this case the optimal defocus TOMBO imager has a FRR = 0.142, which is actually slightly worse than the TOMBO imager with FRR = 0.138. This shows that the MTFs obtained by defocusing (i.e., quadratic phase masks), do not always improve the iris-recognition performance in undersampled imagers. This is mainly due to the reduced optical degrees of freedom offered by defocusing (only one degree of freedom is available: W_D).

It is interesting to consider that compared to the optimized ZPEL imager design with $K = 9$, the design with $K = 16$ yields a small improvement of only 3.4%. The same is true for the TOMBO imaging system where the performance improves by only 3.6% from $K = 9$ to $K = 16$. In fact, the iris-recognition performance achieved by the TOMBO imaging system with $K = 16$ nearly equals that of the conventional imaging system without undersampling, i.e., $F = 1$. This suggests that adding more frames beyond $K = 16$ would not significantly improve the iris-recognition performance, which may first seem counterintuitive. However, recall that increasing the number of frames K also increases the measurement noise variance σ_K^2 as a result of the fixed total photon count constraint, while reducing the effect of aliasing at the same time. Therefore, the resulting trade-off between these two competing processes leads to diminishing improvement in iris-recognition performance with increasing number of frames. As a

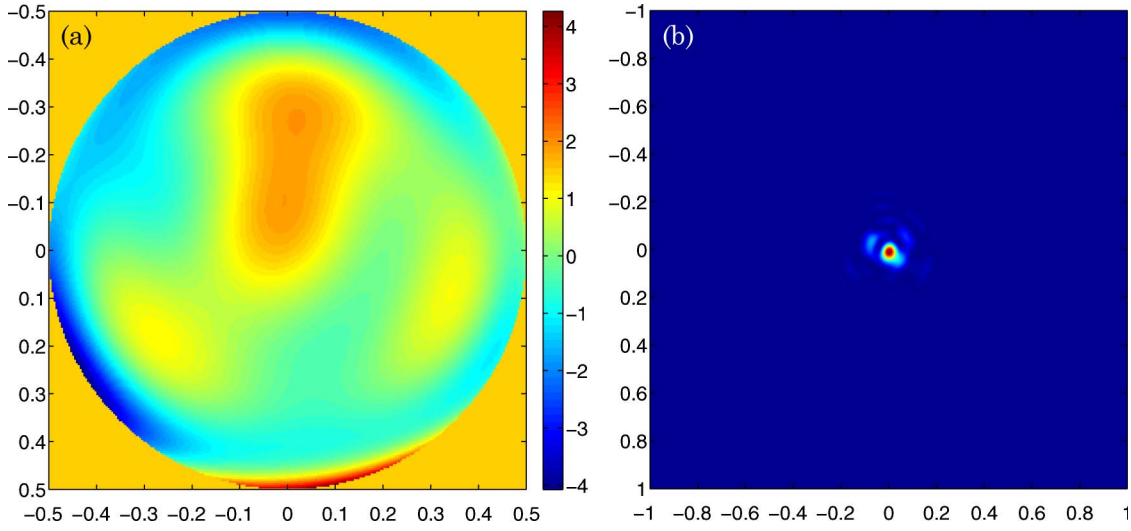

Fig. 12. (Color online) Optimized ZPEL imager with $K = 16$: (a) pupil phase and (b) optical PSF.

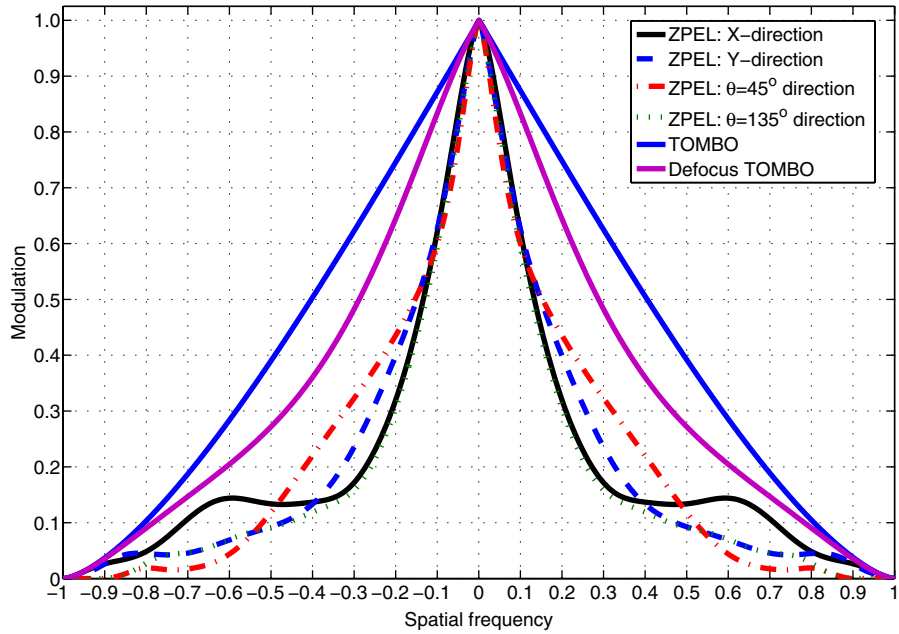

Fig. 13. (Color online) Cross-section MTF profiles of optimized ZPEL imager with $K = 16$.

result, at $K = 16$ the effect of increasing measurement noise nearly counters the reduction in aliasing from the multiple frames, resulting in only a small improvement in FRR for both the ZPEL and the TOMBO imaging systems.

So far we have observed that the optimized ZPEL imager offers a substantial improvement in iris-recognition performance over a TOMBO imaging system with an undersampling detector array. However, these results were obtained using the training dataset, the same dataset that was used in the optimization process. In order to estimate the actual performance of the optimized ZPEL imaging system independent of the training dataset, we need to use a validation dataset. Here we construct a validation dataset consisting of 44 distinct iris subjects with seven samples of each iris, randomly selected from the CASIA database, resulting in a total of 308 iris samples. Figure 14 shows example iris objects from this validation dataset. Note that none of the iris samples in the validation dataset appear in the training dataset. We use a total of 30 noise realizations for each iris object to estimate the FRR from the intraclass and interclass densities. The FRR data for the validation dataset is shown in Table 3. The optimized ZPEL imager with $K = 1$ yields a FRR $=$ 0.138 on the validation dataset as compared to FRR $= 0.164$ for the TOMBO imaging system. This represents a performance improvement of 15.9% over the TOMBO imaging system, which is nearly half of the 32.7% improvement that was obtained with the training dataset. This difference in performance can be explained by considering the fact that the optimization process does not distinguish between the effect of undersampling and the statistics of the particular iris samples comprising the training dataset. As a result, the imaging system is optimized jointly toward mitigating the effect of undersampling and adapting to the statistics of the iris samples in the training dataset so as to minimize the *FRR* metric. Note that the difference between the performance on training and validation dataset will reduce as the size of the training dataset is increased, and it becomes more representative of true iris statistics of the underlying dataset.

In case of $K = 4$, the ZPEL imager achieves a FRR $= 0.0513$, which is an improvement of 19.4% over FRR $= 0.0637$ of the TOMBO imaging system. Note in this case, the improvement obtained with the validation dataset exceeds that obtained with

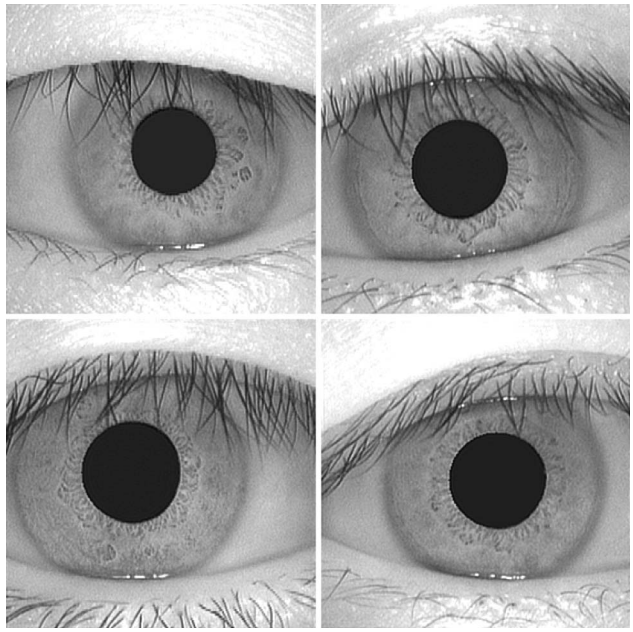

Fig. 14. Iris examples from the validation dataset.

Table 3. Imaging System Performance (FRR) for $K = 1$, $K = 4$, $K = 9$, and $K = 16$ on Validation Dataset

Undersampling	Frames	TOMBO	ZPEL
$F = 1 \times 1$	Conventional imager	0.0543	
$F = 8 \times 8$	$K = 1$	0.1642	0.1383 (15.8%)
$F = 8 \times 8$	$K = 4$	0.0637	0.0513 (19.5%)
$F = 8 \times 8$	$K = 9$	0.0558	0.0444 (20.4%)
$F = 8 \times 8$	$K = 16$	0.0534	0.0440 (17.6%)

the training dataset. With $K = 9$ the optimized ZPEL imager yields a FRR $= 0.0444$ compared to FRR $= 0.0558$ of the TOMBO imaging system. This represents an improvement of 21.6%, which is better than 16.4% improvement obtained on the training dataset. For $K = 16$ frames the optimized ZPEL imager results in FRR $= 0.0534$, a 21.0% reduction from FRR $= 0.0440$ of the TOMBO imaging system with the same number of frames. Note that the FRR of both the optimized ZPEL imager and the TOMBO imaging system do not reduce significantly from $K = 9$ frames to $K = 16$ frames. This is due to the same underlying trade-off between increasing measurement data and increasing measurement noise, which was observed in the case of the training dataset.

5. Conclusions

We have studied the degradation in iris-recognition performance resulting from an undersampling factor of $F = 8 \times 8$ (for the CASIA iris database) and found that in a conventional imager, it yields a FRR $=$ 0.458 compared to a FRR $= 0.133$ when there is no undersampling. We describe an optimization framework that exploits the optical and postprocessing degrees of freedom to maximize the iris-recognition performance in such undersampled imagers. The resulting ZPEL imager design uses an engineered optical PSF together with multiple subpixel shifted measurements to achieve the performance improvement. The ZPEL imager is designed for $K = 1, K = 4$, $K = 9$, and $K = 16$ number of frames. On the training dataset, the optimized ZPEL imager achieved performance improvement of nearly 33% for $K = 1$ compared to the TOMBO imaging system with the same number of frames. With $K = 4$ frames the ZPEL imager design achieved a FRR that is nearly equal to that of a conventional imager without any undersampling. The effectiveness of the optimization framework was also highlighted by the ZPEL imager design with $K = 16$ that achieved a FRR $= 0.113$, which is actually 15% better than FRR $= 0.133$ of the conventional imager without any undersampling. The comparison of the ZPEL imager and the TOMBO imaging system performance using a validation dataset provided further support for the performance improvements obtained on the training dataset. On the validation dataset, the ZPEL imager design required only $K = 4$ frames as opposed to $K = 16$ frames needed by the TOMBO imaging system to equal the performance without undersampling. Similarly, with $K = 16$ frames the optimized ZPEL imager obtained a 21.0% performance improvement over the conventional imaging system without any undersampling. These results demonstrate the power of the task-specific design approach for maximizing the performance of iris-recognition imaging systems in presence of severe detector undersampling. We expect that a good implementation of the ZPEL imager designs would yield an iris-recognition performance close to that predicted by our simulation study. However, as with any physical system implementation, the as fabricated system parameters tend to deviate from their ideal design values. For example, in simulation we assumed ideal uniform subpixel shifts for each frame; however, in a system implementation the actual subpixel shifts achieved would deviate from these ideal values, leading to some degradation in system performance. This issue can be addressed to an extent by carefully estimating the subpixel shifts by using calibration targets and employing these estimate in the iris reconstruction algorithm. In fact, given the various optomechanical fabrication tolerances, a sensitivity and tolerance analysis of the ZPEL imager design can indicate the expected performance of a fabricated system. However, we consider such an detailed analysis as beyond the scope of this study.

Here we considered a security application that operates in "search mode"; however, most security applications operate in "verification" mode and require minimizing FAR while keeping FRR fixed. The optimization framework used in our study can be easily applied for designing iris-recognition systems for such traditional security applications that minimize FAR metric instead. Recall that the segmented optimization approach used in our study does not jointly optimize the optical and postprocessing degrees of freedom, and therefore we expect that there is potential for further performance improvement via a joint-optimization approach [29]. This is a direction of future research that we would like to pursue. Also, the optical parametrization used here assumed that all the subapertures had identical optics; by relaxing this constraint, additional optical diversity can be used to further improve the iris-recognition performance. We would like to quantify such improvements via optical diversity in a future study.

We gratefully acknowledge the financial support of the Defense Advanced Research Projects Agency (DARPA) MONTAGE program. We would also like to thank Dr. Joe van der Gracht for engaging discussions on the subject of undersampling in iris-recognition systems.

References

1. J. G. Daugman, "High confidence visual recognition of persons by a test of statistical independence," IEEE Trans. Pattern Anal. Mach. Intell. **15**, 1148–1161 (1993).
2. J. G. Daugman, "The importance of being random: statistical principles of iris recognition," Pattern Recogn. **36**, 279–291 (2003).
3. J. G. Daugman, "How iris recognition works," IEEE Trans. Circ. Syst. Video Tech. **14**, 21–30 (2004).

4. R. Barnard, V. P. Pauca, T. C. Torgersen, R. J. Plemmons, S. Prasad, J. van der Gracht, J. Nagy, J. Chung, G. Behrmann, S. Mathews, and M. Mirotznik, "High-resolution iris image reconstruction from low-resolution imagery," Proc. SPIE **6313**, 63130D (2006).
5. R. Narayanswamy, P. E. X. Silveira, H. Setty, V. P. Pauca, and J. van der Gracht, "Extended depth-of-field iris recognition system for a workstation environment," Proc. SPIE **5779**, 41–50 (2005).
6. R. Narayanswamy, G. E. Johnson, P. E. X. Silveira, and H. B. Wach, "Extending the imaging volume for biometric iris recognition," Appl. Opt. **44**, 701–712 (2005).
7. D. S. Barwick, "Increasing the information acquisition volume in iris recognition systems," Appl. Opt. **47**, 4684–4691 (2008).
8. V. P. Pauca, D. Chen, J. van der Gracht, R. J. Plemmons, S. Prasad, and T. C. Torgersen, "Pupil phase encoding for multi-aperture imaging," Proc. SPIE **7074**, 70740D (2008).
9. A. Papoulis, "Generalized sampling expansion," IEEE Trans. Circuits Syst. **24**, 652–654 (1977).
10. J. Tanida, T. Kumagai, K. Yamada, S. Miyatake, K. Ishida, T. Morimoto, N. Kondou, D. Miyazaki, and Y. Ichioka, "Thin observation module by bound optics (TOMBO): concept and experimental verification," Appl. Opt. **40**, 1806–1813 (2001).
11. Y. Kitamura, R. Shogenji, K. Yamada, S. Miyatake, M. Miyamoto, T. Morimoto, Y. Masaki, N. Kondou, D. Miyazaki, J. Tanida, and Y. Ichioka, "Reconstruction of a high-resolution image on a compound-eye image-capturing system," Appl. Opt. **43**, 1719–1727 (2004).
12. S. Kay, *Fundamentals of Statistical Signal Processing: Detection Theory* (Prentice-Hall, 1993).
13. CASIA-IrisV1 database, http://www.cbsr.ia.ac.cn/IrisDatabase.htm.
14. J. W. Goodman, *Introduction to Fourier Optics* (McGraw-Hill, 1996), Chap. 7.
15. M. Born and E. Wolf, *Principles of Optics* (Pergamon, 1989), Chap. 9.
16. H. H. Barrett and K. J. Myers, *Foundations of Image Science* (Wiley-Interscience, 2004), Chaps. 7 and 15.
17. H. C. Andrews and B. R. Hunt, *Digital Image Restoration* (Prentice-Hall, 1977).
18. A. Papoulis and S. U. Pillai, *Probability, Random Variables and Stochastic Processes* (McGraw-Hill, 2001).
19. C. L. Fales, F. O. Huck, and R. W. Samms, "Imaging system design for improved information capacity," Appl. Opt. **23**, 872–888 (1984).
20. Y. Itakura, S. Tsutsumi, and T. Takagi, "Statistical properties of the background noise for the atmospheric windows in the intermediate infrared region," Infrared Phys. **14**, 17–29 (1974).
21. N. X. Nguyen, "Numerical algorithms for image superresolution," Ph. D. dissertation (Stanford University, 2000).
22. L. Masek, "Recognition of human iris patterns for biometric identification," Technical report (University of Western Australia, 2003).
23. S. Sanderson and J. Erbetta, "Authentication for secure environments based on iris scanning technology," in *IEE Colloquium on Visual Biometrics* (IEEE, 2000), pp. 8/1–8/7.
24. D. J. Field, "Relations between the statistics of natural images and the response properties of cortical cells," J. Opt. Soc. Am. **4**, 2379–2394 (1987).
25. W. Wenzel and K. Hamacher, "A stochastic tunneling approach for global minimization," Phys. Rev. Lett. **82**, 3003–3007 (1999).
26. MPI 1.1 standard, http://www.mpi-forum.org/docs/mpi-11-html/mpi-report.html.
27. S. Prasad, "Digital superresolution and the generalized sampling theorem," J. Opt. Soc. Am. A **24**, 311–325 (2007).
28. E. Y. Lam, "Noise in superresolution reconstruction," Opt. Lett. **28**, 2234–2236 (2003).
29. M. D. Robinson and D. G. Stork, "Joint digital-optical design of superresolution multiframe imaging systems," Appl. Opt. **47**, B11–B20 (2008).